


 Cite this: *RSC Adv.*, 2023, **13**, 5013

Highly efficient and stable AgI–CdO nanocomposites for photocatalytic and antibacterial activity†

 Murad Z. A. Warshaghah,^a M. Muneer,^{id *a} Ismail I. Althagafi^b and Saleh A. Ahmed^{id *b}

For the last several decades, semiconducting materials and nanocomposites have received a lot of interest in generating highly efficient photocatalysts to destroy organic pollutants and eradicate bacteria. This study uses a simple deposition and precipitation approach at ambient temperature to create a unique and efficient AgI–CdO heterojunction. DRS, IR, SEM, EDS, XRD, EIS, and TEM were utilized to identify the material. SEM and TEM investigation depict the completely spherical, hexagonal forms and zigzag cubes for synthesized AgI–CdO. The EDX spectra reveal the presence of Ag, I, Cd, and O elements without impurity peaks showing that the prepared samples are highly pure. The activity of the synthesized materials was tested by degrading two different chromophoric dyes and a drug derivative (paracetamol) in an aqueous suspension under visible light. In addition, the activity of the most active catalyst was compared with Degussa P25, Fenton's reagent, and under sunlight for degradation of MB and RhB under similar conditions. Photolysis of paracetamol was also looked at using HPLC to identify intermediates formed in the photo-oxidation process. In addition, antibacterial activity was also investigated with the synthesized CdO–AgI nanocomposite *in vitro* against human pathogenic bacterial strains and compared with that of pure materials like AgI and standard ampicillin. The results showed excellent activity with the composite material, which could be due to the higher surface areas and the interactions between AgI and CdO nanoparticles. Quenching investigations revealed O_2^- and holes are principal reactive species. A viable photocatalytic degradation mechanism for organic pollutant elimination over the AgI–CdO nanocomposite has been sketched out based on the obtained results.

 Received 30th November 2022
 Accepted 30th January 2023

DOI: 10.1039/d2ra07626h

rsc.li/rsc-advances

1. Introduction

Contaminants, like pharmaceutical products, metals, and dyes in aquatic systems, pose a hazard to the environment and human health.^{1–8} Different strategies for removing inorganic and organic impurities from water have been developed. Heterogeneous photocatalysis is considered the most environmentally friendly and efficient technology for eliminating these contaminants.^{9–17} Semiconductors, for example, titanium dioxide, zinc oxide, zinc sulfide, and cadmium oxide are widely utilized as photocatalysts for the degradation of organic and inorganic contaminants.^{9,18–21} Semiconductors like TiO₂ and ZnO are the most efficient photocatalysts among these.^{14,19–30} Unfortunately, due to the broad bandgap energy, these materials are active in the UV region and absorb only a tiny percentage of visible light.^{31,32} Researchers have used a variety of

ways to prepare sun-light photocatalysts. One successful technique is to combine two or more narrow gap semiconductors, which may reduce the recombination of electrons–holes and increase the photonic efficiency.^{33–40} Many narrow-bandgap semiconductors containing silver have been employed to prepare influential visible-light-driven photocatalysts over the years, including AgBr,⁴¹ Ag₂O,⁴² AgI,⁴³ Ag₃VO₄,⁴⁴ Ag₂CO₃,⁴⁵ Ag₂S,⁴⁶ Ag₃PO₄,⁴⁷ and Ag₂CrO₄.⁴⁸ AgI has recently been produced in conjunction with other semiconductors, such as ZnO@AgI,⁴⁹ AgI/N-TiO₂,⁵⁰ g-C₃N₄/AgI,⁵¹ AgI/UiO-66(NH₂),⁵² and g-C₃N₄/Ag₃PO₄/AgI, and their photocatalytic performance under visible light has been examined.⁵³ The photocatalytic performance and light absorption ability of metal oxide has been studied in great detail.^{49,54–56} Silver iodide, which has a moderate bandgap in the visible region (2.8 eV), has a strong aptitude for photocatalytic oxidation of various chromophoric organic pollutants.^{57,58} AgI with other photocatalysts is reported to improve charge carrier recombination and absorb light efficiently.^{59–61} Meanwhile, AgI has been deemed a viable material for the creation of a heterojunction system due to its high CB potential (–0.4 eV). Because of these characteristics, AgI could be used as a co-catalyst in the photocatalysis process. As a result, numerous strategies for manufacturing materials by mixing AgI with diverse materials

^aDepartment of Chemistry, Aligarh Muslim University, Aligarh-202002, India. E-mail: m.muneer.ch@amu.ac.in

^bDepartment of Chemistry, Faculty of Applied Sciences, Umm Al-Qura University, Makkah 21955, Saudi Arabia. E-mail: saahmed@uqu.edu.sa

† Electronic supplementary information (ESI) available. See DOI: <https://doi.org/10.1039/d2ra07626h>



for application in photocatalytic pollutant degradation have been developed.^{55–62} In addition, metal oxide-based photocatalysts are also known to possess antimicrobial activity. Numerous substances, like CdO, CaO, and silver-loaded substances, are capable of effectively inactivating microbes by oxidative reaction with ROS.^{63,64} Wang *et al.* examined the different crystal phases of Ag-loaded MnO₂ against *Escherichia coli*.⁶³ Magdalane *et al.* reported the optical, photocatalytic reaction, and antibacterial using CeO₂/CdO nanocomposite with *P. aeruginosa*.⁶⁴

Yang *et al.* have created a metal oxide semiconductor such as Sn₃O₄/PDINH for the photocatalytic production of ROS to kill drug-resistant bacteria.⁶⁵ On the other hand, Wang *et al.* have synthesized a metal-free semiconductor photocatalyst (PDINH/GO) and used it to accelerate wound healing by killing the bacteria and reducing its side effect on the normal tissue cells.⁶⁶ In addition, a metal-free photocatalyst C₃N₄/PDINH has also shown great promise for wound disinfection by inhibiting bacteria growth due to the enhancement of the photocatalytic effect to produce more reactive oxygen species.⁶⁷ These organic–inorganic heterostructures have shown great promise for use in the decomposition of pollutants from water and wound disinfection and killing the bacteria by generating more ROS under irradiation of light and increasing the surface area of these materials.

In the present study, a green co-participation method was used to synthesize highly efficient AgI–CdO nanocomposite, followed by their characterization by different techniques. In the study, we plan to investigate the photocatalytic performance under visible and sunlight and for the first-time antibacterial activity [against (*S. aureus*) (*E. coli* ATCC 25922) and (*P. aeruginosa* ATCC PA01)].

2. Experimental

2.1. Materials used, synthesized materials, materials characterization, trapping experiment, evaluation of photocatalytic study, and *in vitro* antibacterial studies

The details are provided in the attached file.

3. Results and discussion

3.1. XRD analysis

This study has been used to examine the structure and crystallographic phases of pure AgI, CdO, and varying wt% AgI–CdO composites. Fig. 1 depicts the X-ray diffraction pattern of AgI sample, which revealed peaks at 22.34°, 23.73°, 39.19°, 42.63°, and 46.26°. These could be attributed to the crystal planes corresponding to (100), (002), (110), (103), and (112) phases of AgI hexagonal structure.^{49,52,68} The crystallographic planes of CdO's cubic structure are demonstrated by the diffraction peaks of CdO with crystalline planes at 2θ values of 33° (111), 38.6° (200), 55.22° (220), 65.9° (311), and 69.2° (222).^{69–71} Strong and mild diffraction peaks at 2θ values of 18.79°, 29.44°, 35.22°, 49.04°, 52.29°, and 56.08° may be attributable to CdO in synthesized composites (AgI–CdO) with varying wt% AgI. Furthermore, the diffraction peak at 2θ of 22.34°, 23.73°, 39.19°,

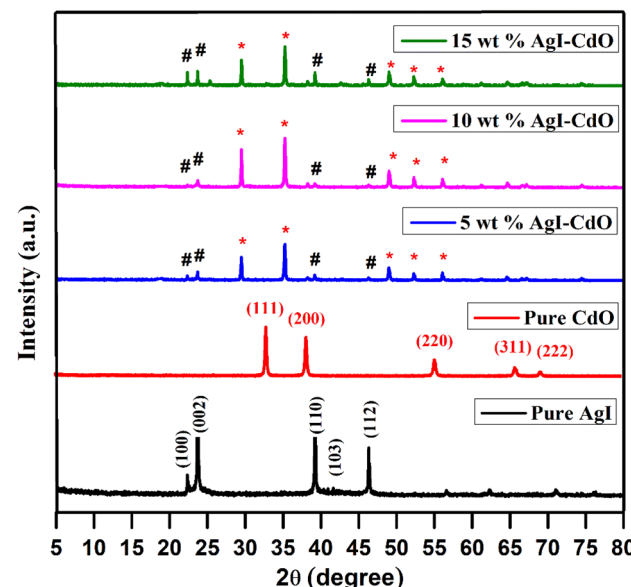


Fig. 1 XRD patterns of bare AgI, CdO, and different wt% AgI–CdO nanocomposite.

42.63°, and 46.26° is unquestionably indexed to AgI. Furthermore, on doping with AgI, the diffraction peaks of CdO were found to shift towards a lower 2θ value, which indicates improvement in the crystallinity. The results also showed the successful formation of composite samples through the integration or substitution of larger atoms by smaller atoms in the lattice.^{72–77}

3.2. FTIR analysis

The distinct functional groups present in the synthesized materials were identified using infrared analysis. The IR spectra of AgI & CdO and composites of these two materials (AgI and CdO) with different weight percent of AgI, are displayed in Fig. S1.† The IR absorption spectrum of AgI showed a broad peak at 3446 & 1624 cm^{−1}, corresponding to the vibrations of H₂O.^{78,79} Whereas, the pure CdO showed an absorption peak at 430 cm^{−1} for Cd=O vibrational modes.^{69,80} On the other hand, all AgI–CdO nanocomposite samples displayed a significant shift with the appearance of a sharp and broad signal at 3600 & 1443 cm^{−1} for O–H. In addition, a small peak at 430 cm^{−1} for Cd=O is shown as a sharp and strong peak in all composite materials.

3.3. Optical studies

This study was made to investigate optical response in the region 200–800 nm. The DRS spectra of pure AgI and CdO, as well as composite samples with various AgI weight percents, are displayed in Fig. 2a. The bare samples of CdO and AgI showed an absorption edge around 605 and 445 nm, respectively.^{49,51,81} The incorporation of AgI onto CdO with the increase in wt% from 5 to 15 led to 6 nm leading to a shift toward a higher wavelength from 447 to 453 nm. The bandgap of different samples was calculated using the Kubelka–Munk eqn (1).^{52,82–84}



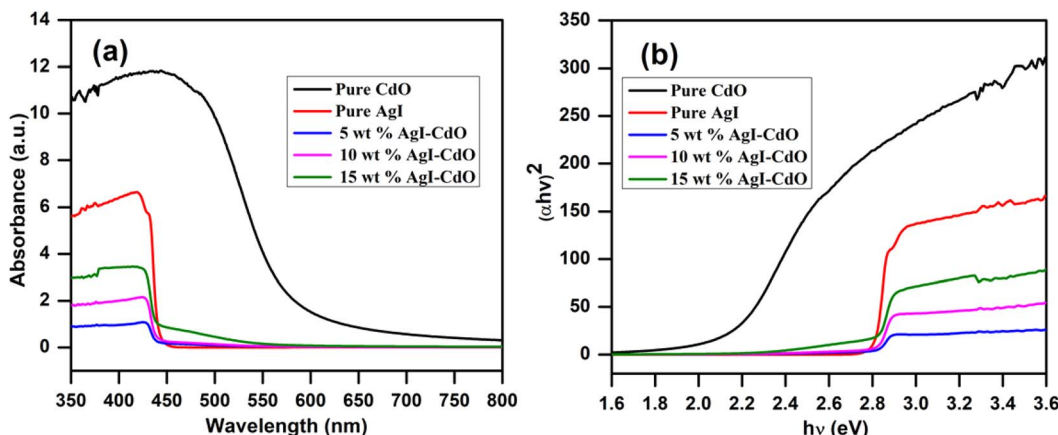


Fig. 2 (a) UV-vis DRS spectra of pure CdO, AgI, and different wt% of AgI doped CdO; and (b) Tauc's plot of synthesis photocatalyst.

$$\alpha h\nu = A (h\nu - E_g)^{n/2} \quad (1)$$

α & h denotes the absorption coefficient and the Planck constant, respectively, ν refers to the light frequency.⁸⁵ The “ n ” for direct and indirect transitions are 1 and 4, respectively.^{51,86} The bandgap (E_g) of pure (CdO and AgI) and nanocomposite (AgI–CdO) was calculated using the plot of $(\alpha h\nu)^2$ vs. $h\nu$, which is shown in Fig. 2b. The calculated bandgap energies for CdO, & AgI were 2 eV, & 2.75 eV. In contrast, all synthesized nanocomposite materials showed values between 2.68 and 2.74 eV.

3.4. SEM study

This study was utilized to analyze the surface structure of all synthesized photocatalysts at higher magnification (0.5 μ m), and images of pure (AgI and CdO) and nanocomposite (10 wt% AgI–CdO) are displayed in Fig. 3. The hexagonal and spherical-shaped as-synthesized pure AgI nanoparticles are seen in Fig. 3a.^{87,88} The bare CdO nanoparticle, on the other hand, has an oval-shaped morphology as observed in Fig. 3b.⁸⁹ The spherical shape of AgI nanoparticles is distributed over the surface of CdO, as evidenced in SEM images (Fig. 3c) of the composite material (10 wt% AgI–CdO).

3.5. EDX and elemental mapping analysis

The results of this study are presented in Fig. 4. Fig. 4a shows two peaks are related to Cd, and O. The presence of Ag and I peaks assigned to the bare AgI nanoparticle is confirmed in Fig. 4b. Fig. 4c shows the EDX analysis of nanocomposite (10 wt% AgI–CdO), which shows all elements (Cd, O, Ag, and I), indicating that the synthesized sample comprises AgI and CdO. The weight percentages of each element present in CdO, AgI, and nanocomposite (10 wt% AgI–CdO) are shown in Fig. 4a–c. EDS elemental mapping results for the distribution of elements are presented in Fig. S2a–h.[†] The elements (Cd, O, Ag, and I) present on the surface of bare CdO (Fig. S2a and b[†]) and AgI (Fig. S2c and d[†]), are uniformly and non-uniformly distributions. Additionally, the elemental mapping of nanocomposite (Fig. S2e–h[†]) reveals a semi-uniform distribution of (Cd, O, Ag, and I) elements, showing that heterojunction nanocomposite has been effectively created.

3.6. TEM analysis

TEM analysis was used to examine the internal morphology of CdO, AgI, and 10 wt% AgI–CdO nanocomposites and their results are displayed in Fig. 5. TEM images of CdO (Fig. 5a) are

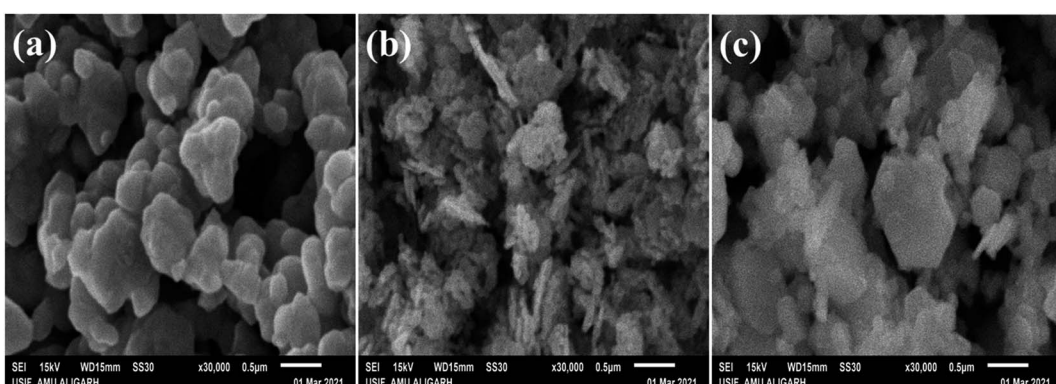


Fig. 3 SEM images of as-prepared pure nanoparticles AgI (a), CdO (b), and heterostructure nanocomposite 10 wt% AgI–CdO (c), at higher magnification.



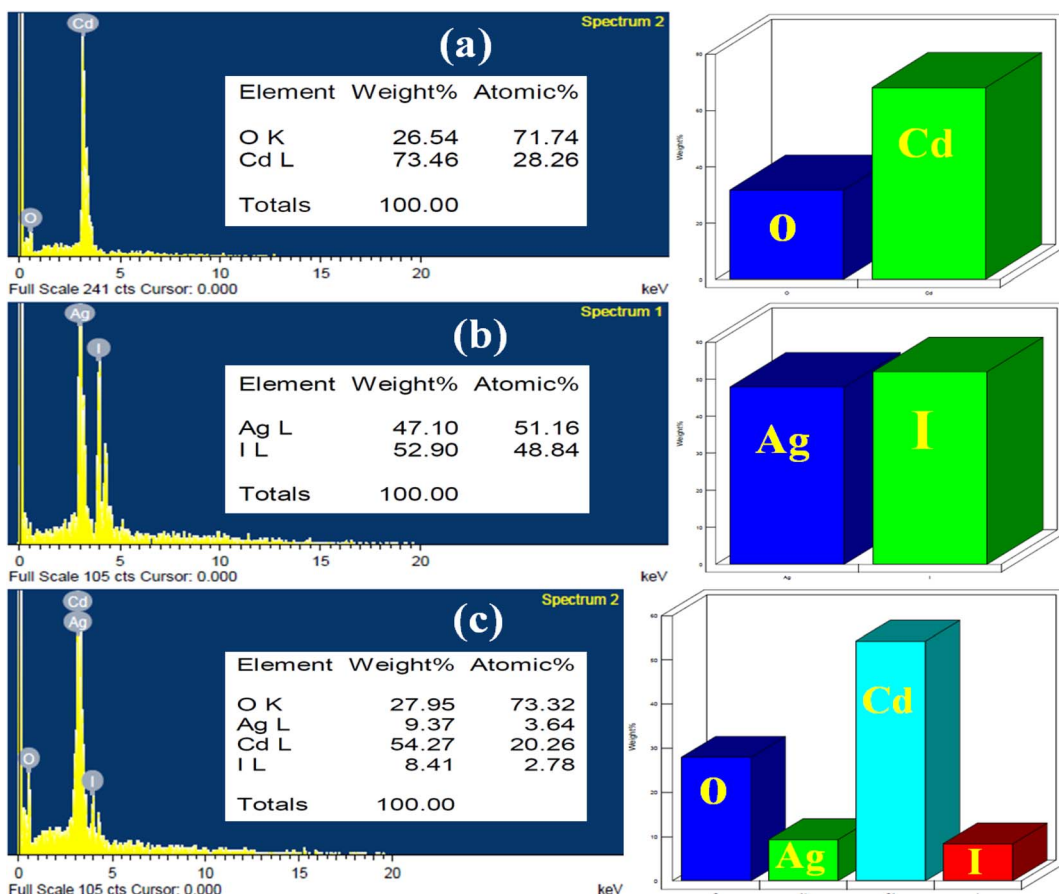


Fig. 4 EDX of as-synthesized photocatalyst, CdO (a), AgI (b), and 10 wt% AgI–CdO nanocomposite (c).

shown as nanospheres with closely attached cubes and hexagonal structures.^{90,91} Whereas, Fig. 5b shows TEM images of AgI nanoparticles in excellent spherical and hexagonal forms. The high-resolution image (insert in Fig. 5b) shows the identification of crystallography. The lattice spacing (0.23 nm) coincides with the (200) plane of AgI. The representative morphology of 10 wt% AgI–CdO heterojunction (Fig. 5c) depicts the dispersion of AgI particles on the surface lattice of CdO, suggesting that the AgI nanoparticles have grown directly on the CdO surface.

3.7. PL study

This study was made to assess the (e^-/h^+) pair recombination rate. Generally, slower charge carrier recombination is thought to imply a lower PL signal.⁸² Fig. 6 depicts the photoluminescence spectrum of all samples at 380 nm excitation in dimethyl sulfoxide from 400 to 650 nm. In comparison to both pure (CdO and AgI) and composite (5 and 15 wt% AgI–CdO), the photoluminescence response of 10 wt% AgI–CdO nanocomposite was found to be the lowest. This suggests that the

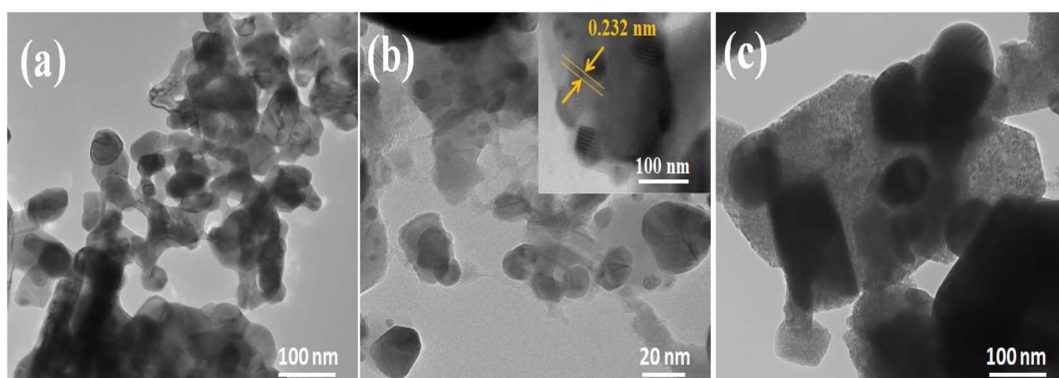


Fig. 5 TEM images of CdO (a), AgI (b), and 10 wt% AgI–CdO (c).



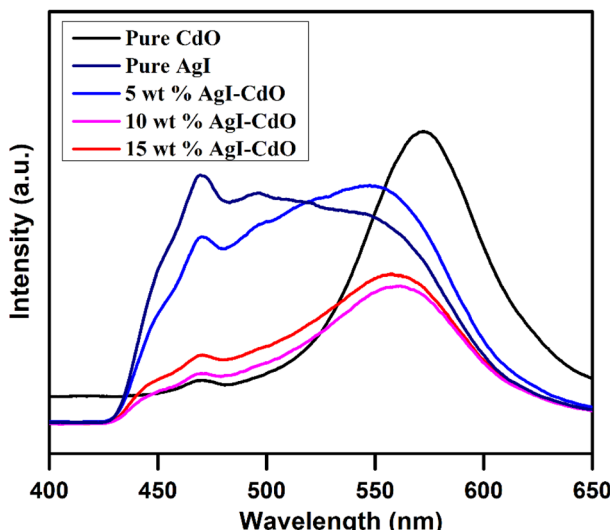


Fig. 6 PL emission spectra of pure CdO, AgI, and varying wt% AgI-CdO nanocomposite in DMSO at an excitation wavelength of 380 nm.

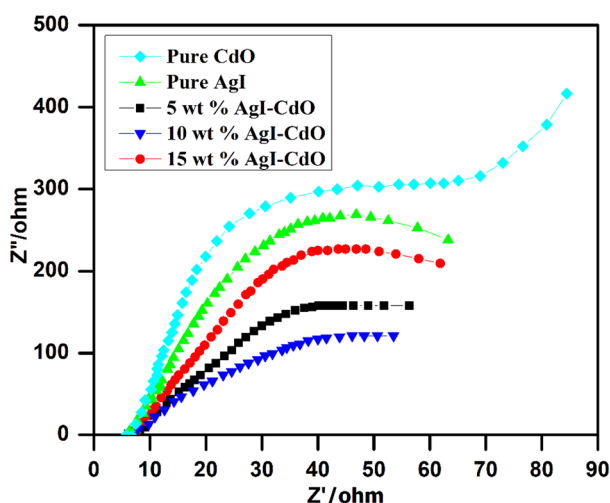


Fig. 7 Nyquist plots of all prepared pure and composite samples.

combined and cooperative of CdO and AgI may reduce the recombination rate of the (e^- and h^+) pair, thereby increasing charged particles for photoreactions, confirming the increased photocatalytic activity of AgI-CdO nanocomposite materials.

3.8. EIS analysis

The photogenerated charge separation is a critical factor in photocatalytic reactions. Electrochemical impedance spectroscopy (EIS) is a technique for determining the efficiency with which electron-hole pairs are separated. The charge-transfer resistance is inversely proportional to the semicircle diameter.^{79,83} The Nyquist impedance spectra of CdO, AgI, 5 wt% AgI-CdO, 10 wt% AgI-CdO, and 15 wt% AgI-CdO photocatalyst are shown in Fig. 7. The photocatalyst, 10 wt% AgI-CdO composite showed small semicircle among all samples, inferring the lowest charge transfer resistance. This demonstrates that the prepared AgI-CdO heterostructure has significantly improved electron/hole separation and charge transfer efficiency, which is beneficial in photocatalysis. This conclusion is consistent with the findings of the PL analyses.

3.9. Photocatalytic degradation study

The photocatalytic efficiency of prepared nanoparticles was determined by illuminating desired compound (aqueous solution of RhB, MB, as well as paracetamol) under a visible light source in the presence of air bubbling. Before illumination, the photocatalyst and the desired compound (RhB, MB, and paracetamol) were kept in the dark for 30 min with constant stirring to get absorption-desorption equilibrium. Fig. 8a and b show the UV-vis spectrum of MB and RhB over 10 wt% AgI-CdO nanocomposite with respect to time, demonstrating 93–99% degradation in 77 min, respectively.

Fig. 9a and b show a decrease in concentration *vs.* irradiation time for MB and RhB with & without catalysts. Without a catalyst, the photodegradation of MB and RhB was insignificant implying that the compounds are quite stable and cannot be destroyed by direct photolysis. It's also worth noting that the 10 wt% AgI-CdO decomposes both dyes (RhB and MB) more

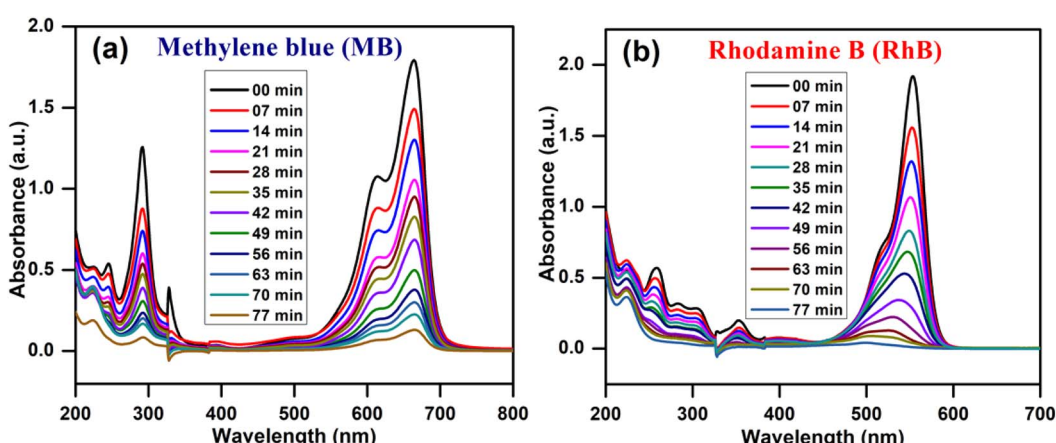


Fig. 8 Decrease in absorbance on irradiation of MB (a) & RhB (b) over 10 wt% AgI-CdO at various times under light.

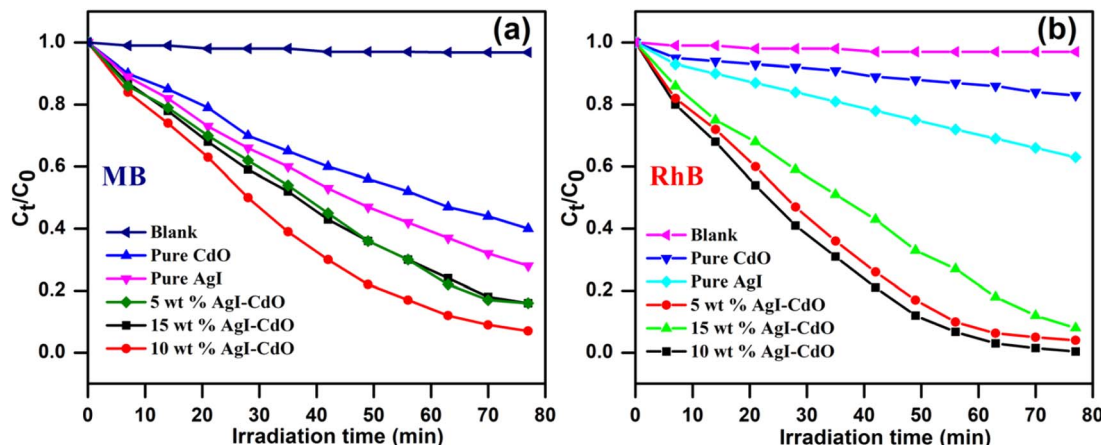
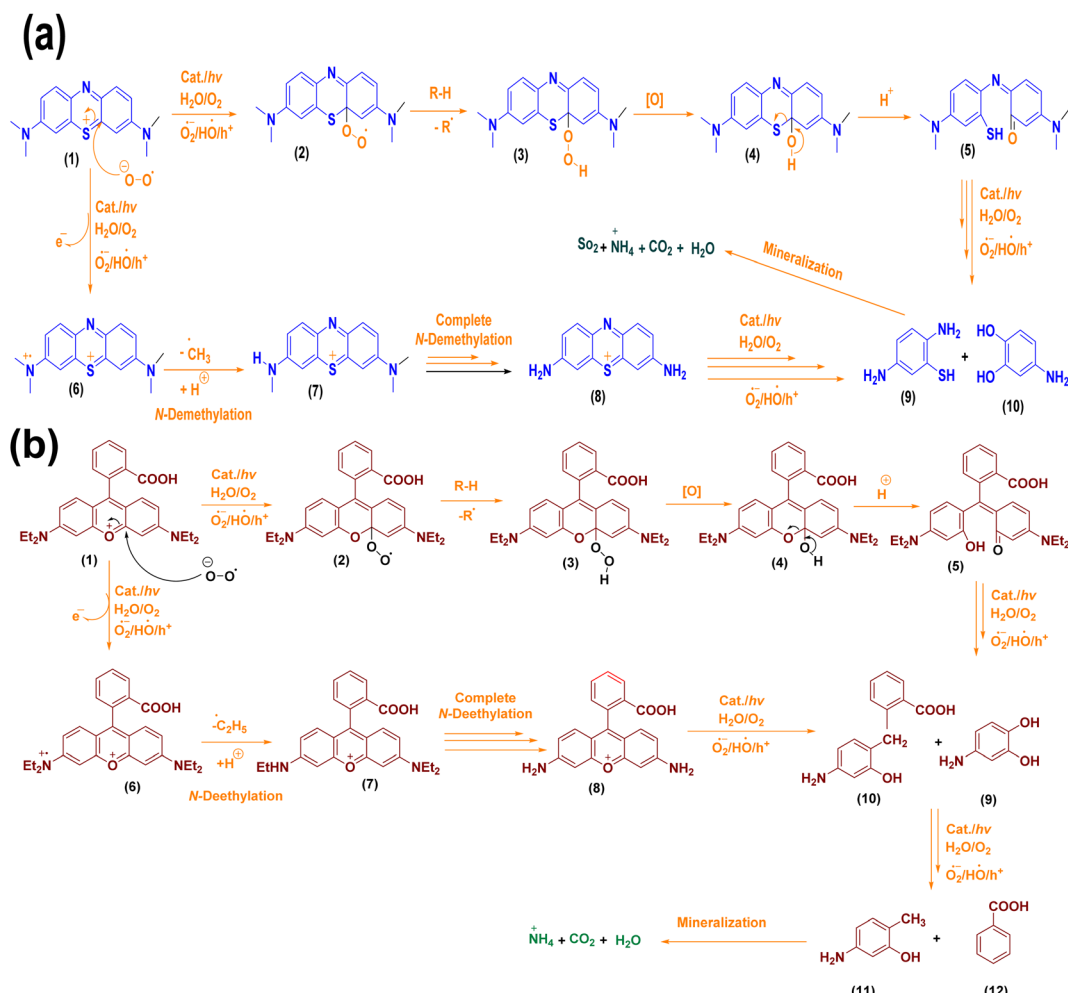


Fig. 9 Photodegradation of MB (a) & RhB (b) with and without catalyst under light.

quickly than any other produced catalyst. This may be due to the joint effect of AgI and CdO at this concentration, which may lead to sufficient light absorption & the separation of photo-generated charge carriers.

A mechanism for the decomposition of dyes in the presence of synthesized catalysts is given in Scheme 1a and b, showing the reaction of dyes with O_2^\cdot , HO^\cdot , and h^+ produced in the medium. As both dye derivatives have positive charges and are



Scheme 1 (a and b) Possible mechanistic route for the breakdown of dyes.



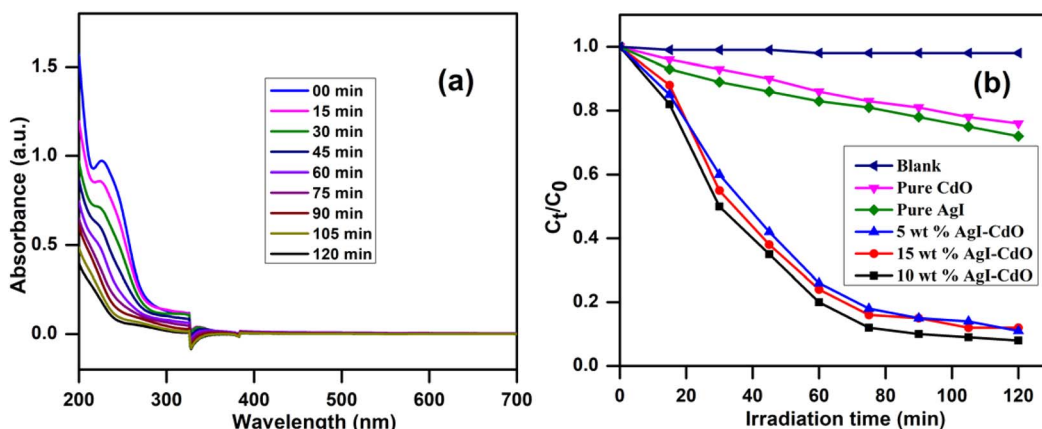


Fig. 10 (a) Decrease in absorbance of paracetamol at different time with visible light over 10 wt% AgI–CdO heterojunction nanocomposite, and (b) concentration change vs. time in the absence and presence of different photocatalysts.

cationic dyes, the superoxide radical anion would be the most vulnerable kind of attack. As indicated in the following Scheme 1a and b, the dye derivatives undergo a further reaction with reactive species produced in the reaction media that ultimately mineralizes into non-toxic components after dealkylation and fragmentation.

Additionally, the efficacy of the photocatalyst, 10 wt% AgI–CdO was assessed by studying the decomposition of a colorless organic compound such as a drug derivative (paracetamol) in aquatic suspension. Fig. 10a shows the paracetamol absorption spectra with time at its λ_{max} (243 nm) during the decomposition process with 10 wt% AgI–CdO heterojunction nanocomposite, which shows a decrease in absorbance with irradiation time, showing 91.3% removal in 120 min. Fig. 10b displays the change in concentration of paracetamol vs. illumination time in the presence and absence of various photocatalysts. It's also worth noting that the paracetamol is degraded faster with the catalyst, 10 wt% AgI–CdO, compared with other prepared pure and composite materials. The excellent effect of the 10 wt% AgI–CdO nanocomposite for paracetamol elimination could be attributed to the efficient separation of charge carriers in heterojunction and good light absorption.

HPLC analysis was utilized to analyze the generated intermediates in the photodegradation of paracetamol over 10 wt% AgI–CdO. The HPLC peak of starting compound ($R_t = 3.09$ and 4.01 min) significantly decreases with time, and the paracetamol was removed within 120 min, as displayed in Fig. S3.† Besides, no by-products are found as detected in the time-dependent HPLC analysis of paracetamol under analogous conditions.

3.10. Photocatalytic degradation of RhB and MB under sunlight

The photocatalytic proficiency of synthesized AgI–CdO was also performed under sunlight (light intensity of $116 \mu\text{W cm}^{-2}$) under identical conditions using the same reaction vessel. Under this experiment, an aqueous solution of RhB or MB was taken in an immersion well photochemical reactor in the

presence of a catalyst. The solution was illuminated under sunlight with proper cooling and stirring. The samples were taken at various time intervals, and spectrophotometric were monitored for degradation. A control experiment was carried out under identical conditions without a catalyst. The absorbance change at a different time on the illumination of RhB and MB under sunlight in the presence and absence of a catalyst is displayed in Fig. S4a–d.† The figure showed no appreciated change in the absence of a catalyst, whereas 85% and 94.3% degradation of MB and RhB could be seen in 180 and 210 min, respectively. The results suggest that the produced material is efficient in eliminating dyes under sunlight, which is quite promising from an application point of view.

3.11. Comparative degradation with another oxidative process (photo-Fenton and Degussa P25 TiO₂)

The activity of the synthesized photocatalyst (10 wt% AgI–CdO) was compared with the photo-Fenton process and commercially available Degussa P25 TiO₂, by studying the removal of RhB and MB under similar conditions. Fig. 11 displays the concentration change vs. time on the illumination of MB and RhB with Degussa P25, Fenton's reagent, and the synthesized catalyst (10 wt% AgI–CdO) with visible light. The figure indicates better performance of the prepared catalyst for the decomposition of both dyes, exhibiting 93% and 99.5% degradation for MB and RhB in 77 min. In contrast, only 41–54% and 80.4–84% degradation was observed in the presence of P25 and Photoenton reagent, respectively.

3.12. Degradation kinetics of RhB & MB

The degradation rate of MB and RhB was calculated using pseudo-first-order kinetics using the following eqn (2).

$$\ln(C_0/C_t) = k_{\text{app}}t \quad (2)$$

C_0 and C_t are the starting and final dye concentrations at $t = 0$, and the final irradiation period; k is the first-order rate constant. Fig. 12a and b, respectively exhibit a plot of $-\ln(C_0/C_t)$



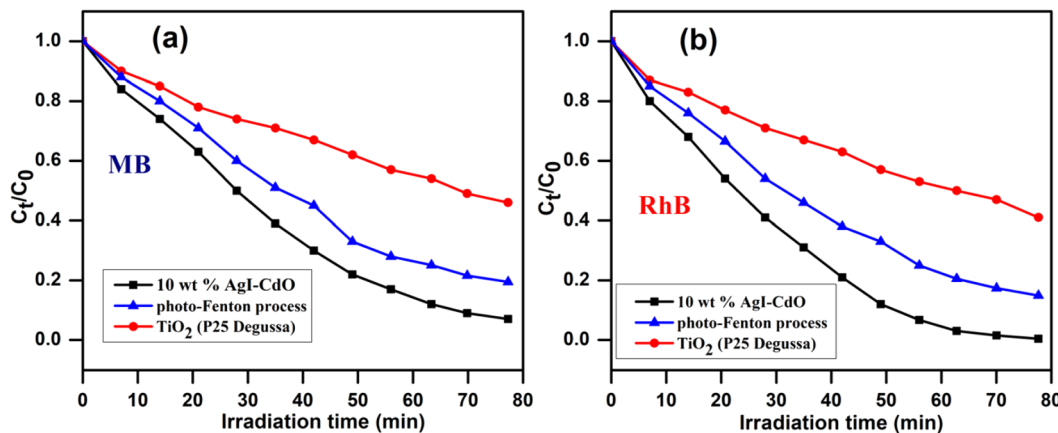


Fig. 11 Time-dependent variation in the concentrations of MB (a) & RhB (b) on illumination with visible light in the presence of Fenton's reagent, Degussa P25, and synthesized photocatalyst (10 wt% AgI–CdO) under analogous conditions.

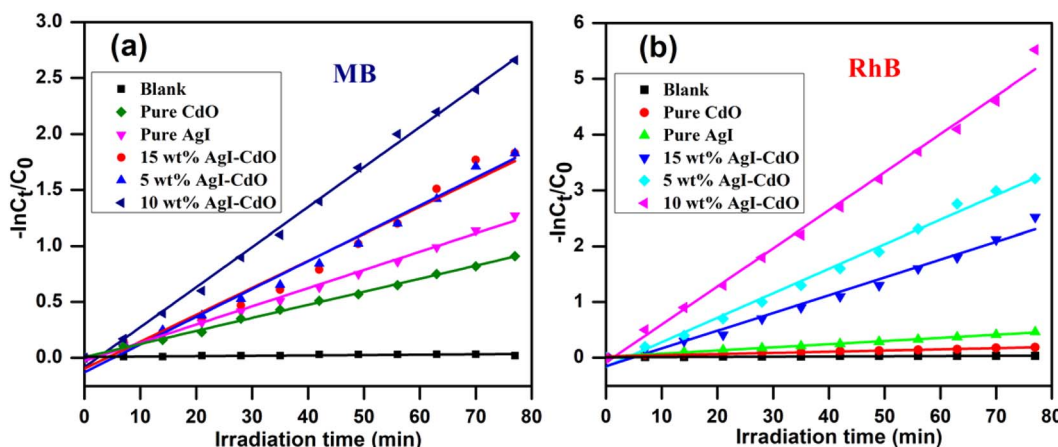


Fig. 12 The pseudo-first-order cure fit shows the plot of $-\ln C_t/C_0$ vs. irradiation time for the elimination of MB (a) & RhB (b) with various catalysts under a visible light source.

vs. irradiation time displaying linear curve fit for eliminating MB and RhB utilizing pure AgI, CdO, and AgI–CdO heterojunction of nanocomposites with varied wt% of AgI. These figures were used to calculate the rate constant (k_{app} value) and correlation coefficients (R^2) for dye degradation with and

without catalysts. The results are summarized in Table 1. The k_{app} value for 10 wt% AgI–CdO nanocomposite was higher than all other synthesized photocatalysts. The results suggest that as the loading of AgI onto CdO increases from 5 to 10 wt%, the removal of MB and RhB increases, and a further increase in the amount of AgI loading resulted in a reduced photocatalytic response. This may be due to as the AgI loading increases, the charge carrier separation may be suppressed. Accordingly, from all the synthesized photocatalysts, 10 wt% AgI–CdO nanocomposite is found to be the most active catalyst for MB & RhB removal.

Table 1 Pseudo-first-order rate constants of all the synthesized photocatalysts and their corresponding R^2 values for the elimination of MB and RhB

Sample	Apparent rate constant (k_{app}) (min^{-1})		R^2	
	MB	RhB	MB	RhB
Blank	3.306×10^{-4}	3.696×10^{-4}	0.6193	0.8026
CdO	0.0117	0.0020	0.9979	0.9705
AgI	0.0160	0.0050	0.9956	0.9957
5 wt% AgI–CdO	0.0240	0.0400	0.9719	0.992
15 wt% AgI–CdO	0.0240	0.0310	0.9846	0.9819
10 wt% AgI–CdO	0.0357	0.0680	0.9968	0.9936

3.13. Reusability and stability

From the standpoint of application, photocatalyst reusability is crucial in determining the catalyst's stability. As a result, the recycling process was investigated using recovered catalysts from the irradiated mixture of RhB under comparable conditions to assess the stability of the most active material (10 wt% AgI–CdO). The catalyst was collected and rinsed several times with ethanol and then with water to eliminate undesirable



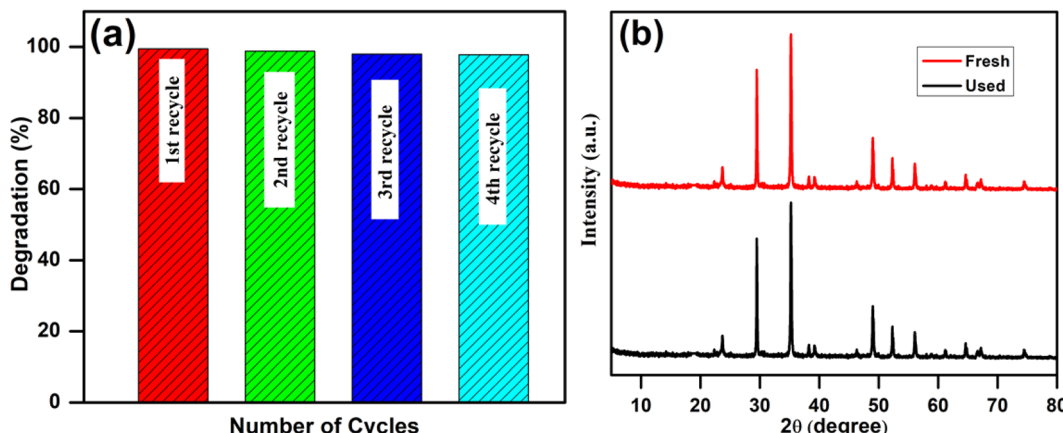


Fig. 13 (a) Recyclability of a 10 wt% AgI–CdO photocatalyst for the removal of RhB after four cycles, and (b) XRD of 10 wt% AgI–CdO before and after the photolysis experiment.

components and dried at 100 °C overnight before applying for the next cycle. Fig. 13a shows the % dye degradation after four consecutive cycles showing no change in catalyst photocatalytic activity. Additionally, there were no differences in the crystal structure of the catalyst (10 wt% AgI–CdO) according to XRD studied before and after the photocatalytic experiment. According to the results, the synthesized nanocomposite (10 wt% AgI–CdO) has high stability for eliminating organic contaminants from water and may be employed after numerous photocycle under visible light.

3.14. Antibacterial activity

The agar method was used to examine the anti-bacterial activities of the prepared nanoparticles against Gram-positive bacteria (*S. aureus*) and Gram-negative bacteria (*E. coli* ATCC 25922 and *P. aeruginosa* ATCC PA01). Ampicillin and DMSO were utilized as the positive and negative control, respectively. Based on the antimicrobial assay performed to assess the antagonistic activity of CdO, AgI, and AgI–CdO nanocomposite against bacterial, it was noted that AgI–CdO exhibited a promising antagonistic influence at the concentration of 100 mg l⁻¹ against (*S. aureus*) (*E. coli* ATCC 25922) and (*P. aeruginosa* ATCC PA01). Moreover, it was observed that AgI–CdO shows closely equivalent bactericidal potential as compared to the pure CdO NPs Table 2. In addition, AgI–CdO nanocomposite has shown

admirable antibacterial activity against Gram-positive and Gram-negative pathogenic strains compared with pure AgI and standard drug ampicillin Table 2. Among the three different catalysts, bactericidal activity varied in the order of AgI–CdO > CdO > AgI, which might be due to the high surface area and light response and the interactions between AgI and CdO nanoparticles and the generation of ROS. An inhibition zone measurement was performed to test the activity of synthesized catalysts. Fig. 14 shows that no inhibition zone was formed around the AgI and DMSO. While, the AgI–CdO displayed the highest inhibition zone as compared to bare samples, with a diameter around 21 mm, 22 mm, and 29 mm against (*S. aureus*) (*E. coli* ATCC 25922) and (*P. aeruginosa* ATCC PA01) respectively, indicating that AgI–CdO visibly restrained the proliferation of bacteria. The results suggested that AgI–CdO played an important role in killing bacteria and that our synthesized nanocomposite could be used as an anti-bacterial agent.

3.15. Quenching experiments

The scavengers such as BQ, EDTA-2Na, and IPA were used in the photodegradation reaction of the dye under analogous conditions to trap the primary active species [O₂^{·-}, h⁺, and 'OH] involved for the removal of compounds under investigation. Fig. 15 shows the percent degradation of RhB on irradiation an

Table 2 Tabulation displaying the inhibitory effect of CdO, AgI, and nanocomposites on *P. aeruginosa*, *S. aureus*, and *E. coli*

Sample	Zone of inhibition (mm) at different concentrations against three pathogenic strains					
	Concentration (100 mg mL ⁻¹)		Concentration (50 mg mL ⁻¹)			
	<i>P. aeruginosa</i>	<i>S. aureus</i>	<i>E. coli</i>	<i>P. aeruginosa</i>	<i>S. aureus</i>	<i>E. coli</i>
CdO	28	19	20	27	19	20
AgI	14	NIL	NIL	12	NIL	NIL
AgI–CdO	29	21	22	29	20	20
Ampicillin	14	13	20	16	13	19

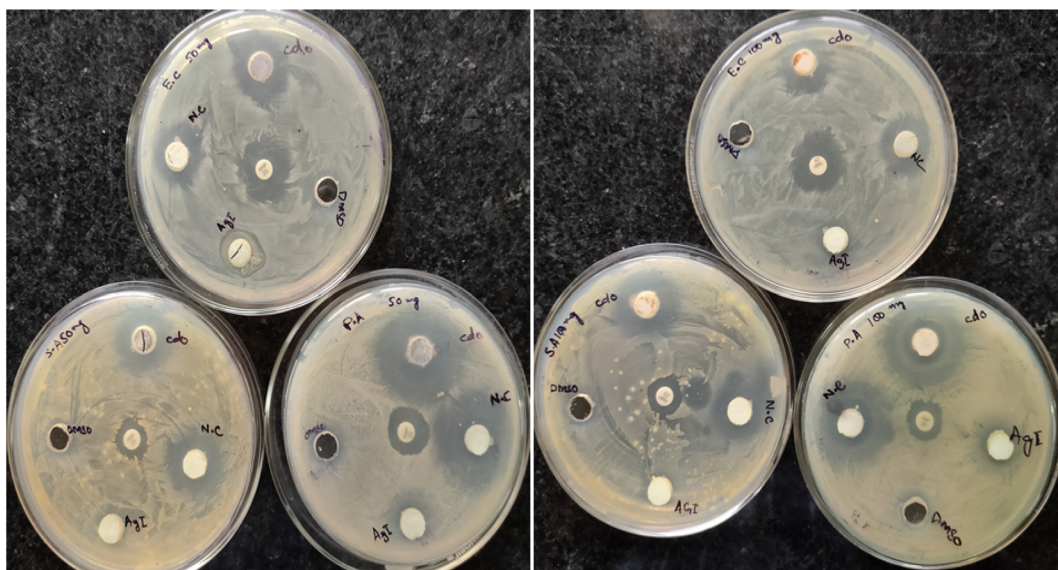


Fig. 14 Zone inhibition image of *P. aeruginosa*, *S. aureus*, and *E. coli*. in the presence of CdO, AgI, and nanocomposites at different two concentrations of 50 and 100 mg l⁻¹.

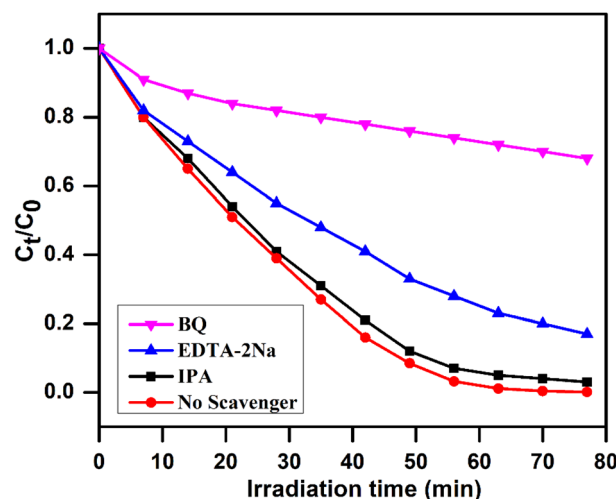


Fig. 15 Concentration change vs. time on irradiation of rhodamine B in an aqueous medium over 10 wt% AgI–CdO nanocomposite with and without quenchers.

aqueous solution under visible light with 10 wt% AgI–CdO using the above mentioned quenchers under comparable conditions. The scavenger BQ significantly reduces RhB degradation, whereas EDTA-2Na showed a minor influence. Moreover, the addition of IPA did not affect the degradation of RhB, indicating $\cdot\text{O}_2$ & h^+ are the key reactive species involved in the reaction.

In addition, the terephthalic acid (TA) fluorescence probe method was used to monitor hydroxyl radical-derived products formed in the photoreaction in a basic medium with a catalyst. The 2-hydroxyterephthalic acid (TA-OH) is thought to be produced when the hydroxyl radicals ($\cdot\text{OH}$) react with terephthalic acid and show a strong fluorescence peak (PL signal) at

425 nm, which was monitored at different time intervals.^{49,51} The commercially available TiO₂ (Degussa, P25) was used as a standard catalyst to monitor this reaction under similar conditions. Fig. 16 shows the photoluminescence spectral change observed on irradiating an alkaline terephthalic acid solution (at excitation 315 nm) with Degussa P25 (Fig. 16a) and a 10 wt% AgI–CdO nanocomposite (Fig. 16b). Fig. 16a shows that the photoluminescence signal gradually increases with irradiation time over Degussa P25, indicating that hydroxyl radicals are involved in the reaction to form TA-OH. However, the photoluminescence signal was not found to increase in the presence of 10 wt% AgI–CdO nanocomposite (Fig. 16b), indicating that no $\cdot\text{OH}$ was produced under this condition. This concluded that the trapping experiment results are in agreement with these results.

3.16. Degradation mechanism

The band potential is an intrinsic feature of semiconducting materials that dictates the mechanism of these reactions. To elucidate the mechanism of (e^-/h^+) pairs generated on excitation of 10 wt% AgI–CdO nanocomposites, CB & VB potentials of produced pure materials (AgI and CdO) were computed using eqn (3) and (4).⁷⁹

$$E_{\text{VB}} = X - E^{\text{e}} + 1/2E_{\text{g}} \quad (3)$$

$$E_{\text{CB}} = E_{\text{VB}} - E_{\text{g}} \quad (4)$$

E^{e} = free-electron energy, X = electronegativity on the hydrogen scale (ca. 4.5 eV).

The mean of the 1st ionization energy (eV) and the electron affinity was used to calculate the absolute electronegativity (eV). The terms E_{VB} , E_{CB} , and E_{g} refer to the semiconductor's, VB & CB potential and bandgap energy, respectively.



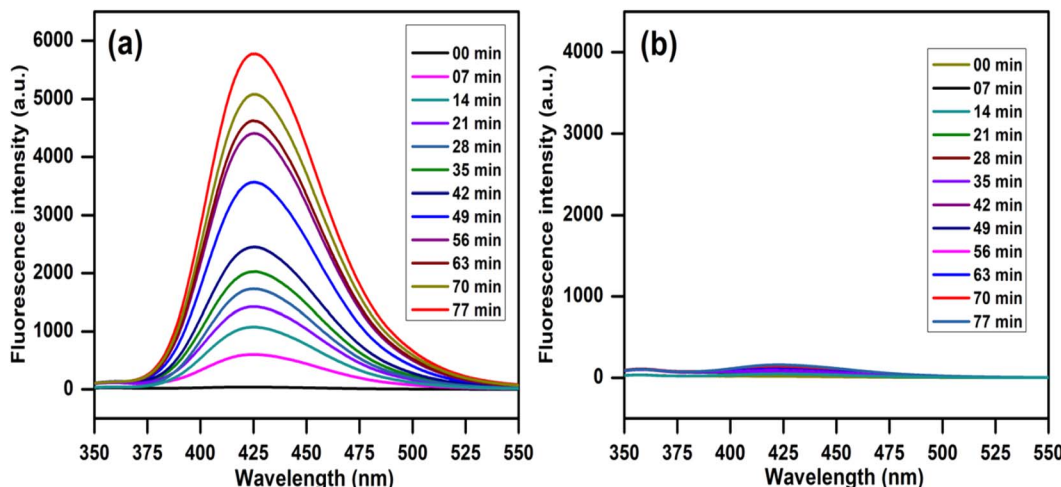
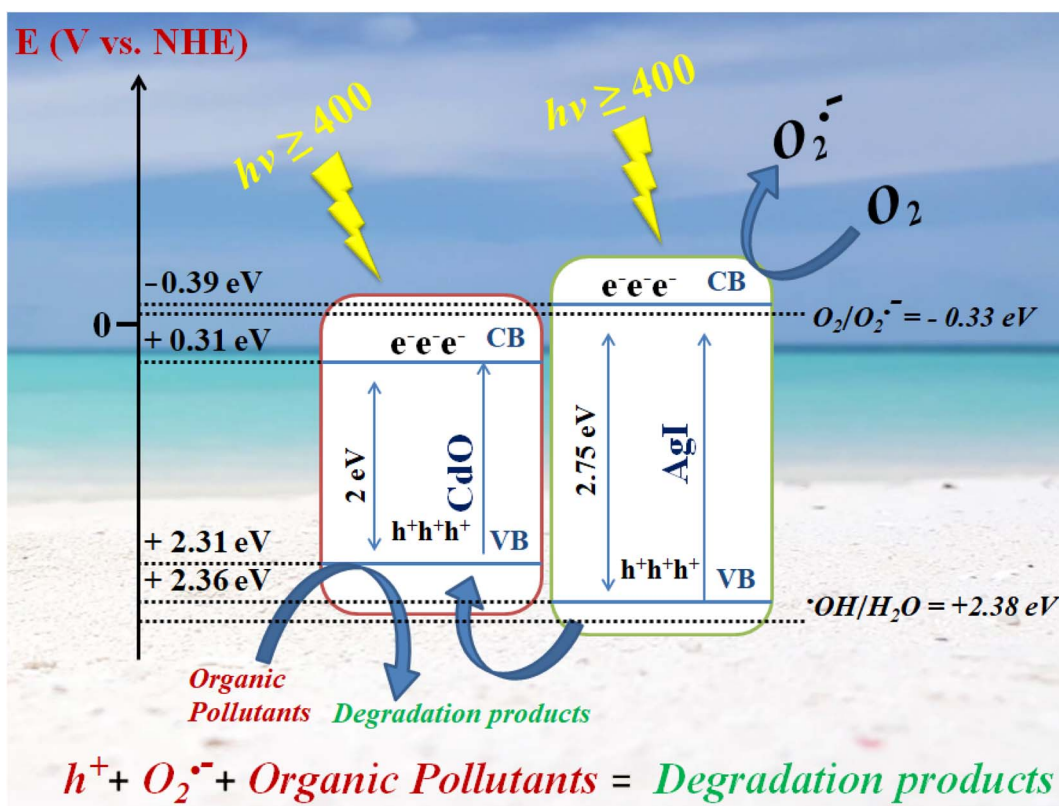


Fig. 16 PL spectrum observed on irradiation of a 5×10^{-4} M alkaline TA solution (at λ_{exc} 315 nm) with (a) TiO_2 and (b) 10 wt% $\text{AgI}-\text{CdO}$ nanocomposite photocatalyst.

CdO 's VB and CB energies were found to be +2.31 eV and 0.31 eV, while AgI 's are +2.36 eV & -0.39 eV. The bandgap energies of CdO & AgI have been calculated to be 2 eV and 2.75 eV. A plausible photocatalytic mechanism for the breakdown of compounds under investigation catalyzed by $\text{AgI}-\text{CdO}$ is postulated in Scheme 2 based on the previous results. The electrons in VB of CdO and AgI can easily be excited to their CB when exposed to visible light, resulting in the creation of holes in their VBs (eqn (5) and (6)). Furthermore, AgI 's CB energy level

(-0.39) is more negative than the potential of $\text{O}_2/\text{O}_2^{\cdot-}$ (-0.33 eV),⁵¹ the electrons in the CB of AgI can be trapped by dissolved molecular oxygen to generate $\text{O}_2^{\cdot-}$ (eqn (7)) leading to improved photocatalytic efficiency (eqn (8)). The VB of AgI (+2.36 eV) is greater than that of CdO (+2.31 eV), thus holes generated can be transported into CdO 's VB (eqn (9)) and react directly with organic compounds, resulting in the complete of degradation (eqn (10)).

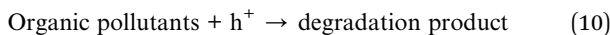
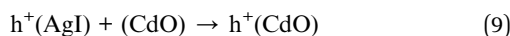
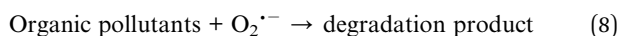
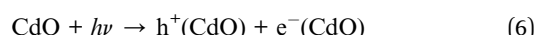
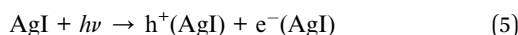


Scheme 2 A proposed mechanism for decomposition of organic pollutants by $\text{AgI}-\text{CdO}$ photocatalyst under sun/visible light irradiation.

The transformation of $\cdot\text{OH}$ from H_2O has a potential of $+2.38$,^{49,51} higher than CdO and AgI 's VB potentials. As a result, the photoinduced h^+ in the VB of CdO & AgI cannot oxidize the water molecule to give $\cdot\text{OH}$, which is in agreement with the PL results that $\cdot\text{OH}$ is not observed using AgI-CdO as a catalyst when exposed to light. This is in line with the results of the trapping experiment.

The photogenerated carriers can be successfully segregated in this route, resulting in significantly increased photocatalytic activity. These findings are consistent with PL and UV-vis data, and increased photocatalytic activity is attributable to increased light-harvesting capacity and the ability to produce and move excited charge carriers.

The sequential representation of the generation of reactive species on irradiated semiconductors in aqueous suspension and its further reaction with organic pollutants is represented below;



4. Conclusions

In conclusion, AgI-CdO nanocomposites were successfully produced at room temperature using a simple deposition cum precipitation process and employed for the photodegradation of MB, RhB, and paracetamol. The nanocomposite materials performed better activity compared to bare CdO and AgI . The performance of the most active catalyst (10 wt% AgI-CdO) was compared with Degussa P25, Fenton's reagent, and also under sunlight for dye degradation under the same conditions. According to the scavenger studies and the TA-OH probe experiment, hydroxyl radicals ($\cdot\text{OH}$) play a minor role, whereas superoxide radicals ($\text{O}_2\cdot^-$) is the main reactive species in the photooxidation process. The heterojunction nanocomposites formed between CdO and AgI can collectively minimize the e^- and h^+ pair recombination rate, resulting in a greatly improved separation efficiency, which is responsible for high photodegradation activity. *In vitro* antibacterial studies revealed that the AgI-CdO showed the highest antibacterial efficacy against (*S. aureus*) (*E. coli* ATCC 25922) and (*P. aeruginosa* ATCC PA01) with zone inhibition 21 mm, 22 mm, and 29 mm respectively compared with standard drug and pure AgI . This could be due to the interactions between AgI and CdO nanoparticles and the generation of ROS. The present study demonstrates a straightforward, effective, and simple approach to synthesizing highly efficient visible-light active catalysts for the removal of

pollutants in water systems and the photodynamic treatment of pathogenic bacterial strains. Moreover, this approach also offers a number of advantages, such as the use of solar light, less reaction time, small catalyst concentration, high degradation efficiency, air as the oxidant, as an anti-bacterial agent, and ease of catalyst recycling.

Conflicts of interest

There are no conflicts to declare.

Acknowledgements

The authors are thankful to the SERB Project (CRG/2019/001370), DST, and UGC for DRS II, PURSE & FIST for their support to the chemistry department at AMU, Aligarh. The authors would like to acknowledge the Deanship of Scientific Research at Umm Al-Qura University, for supporting this work by Grant code: 22UQU4320545DSR30. Murad Z. A. Warshagh expresses gratitude to ICCR for providing financial support for his PhD program.

References

- 1 N. Sharotri, D. Sharma and D. Sud, *J. Mater. Res. Technol.*, 2019, **8**, 3995–4009.
- 2 A. Shet and S. K. Vidya, *Sol. Energy*, 2016, **127**, 67–78.
- 3 D. Yu, J. Bai, H. Liang and C. Li, *J. Alloys Compd.*, 2016, **683**, 329–338.
- 4 D. Yu, J. Bai, H. Liang, J. Wang and C. Li, *RSC Adv.*, 2015, **5**, 91457–91465.
- 5 O. O. Alameer, A. Timoumi, N. El Guesmi, S. N. Alamri, W. Belhadj, K. Althagafi and S. A. Ahmed, *Eur. Phys. J. Plus*, 2022, **137**, 1160.
- 6 M. M. Kaid, A. S. Khder, S. A. Ahmed, A. A. Ibrahim, H. M. Altass, R. I. Alsantali, R. S. Jassas, M. A. Khder, M. M. Al-Rooqi, Z. Moussa and A. I. Ahmed, *ACS Omega*, 2022, **7**, 17223–17233.
- 7 C. Nefzi, B. Askri, B. Yahmadi, N. El Guesmi, J. M. García, N. Kamoun-Turki and S. A. Ahmed, *J. Photochem. Photobiol. A: Chem.*, 2022, **431**, 114041.
- 8 C. Nefzi, B. Yahmadi, N. El Guesmi, J. M. García, N. Kamoun-Turki and S. A. Ahmed, *J. Mol. Struct.*, 2022, **1251**, 131943.
- 9 A. Pramothkumar, N. Senthilkumar, K. C. M. G. Malar, M. Meena and I. V. Potheher, *J. Mater. Sci.: Mater. Electron.*, 2019, **30**, 19043–19059.
- 10 J. Di, J. X. Xia, M. Ji, B. Wang, S. Yin, Q. Zhang, Z. Chen and H. Li, *Appl. Catal., B*, 2016, **183**, 254–262.
- 11 J. Xia, J. Di, H. Li, H. Xu, H. Li and S. Guo, *Appl. Catal., B*, 2016, **181**, 260–269.
- 12 J. Jin, Q. Liang, C. Ding, Z. Li and S. Xu, *J. Alloys Compd.*, 2017, **691**, 763–771.
- 13 F. Zhang, Q. Wen, M. Hong, Z. Zhuang and Y. Yu, *Chem. Eng. J.*, 2017, **307**, 593–603.
- 14 Y. Tang, H. Zhou, K. Zhang, J. Ding, T. Fan and D. Zhang, *Chem. Eng. J.*, 2015, **262**, 260–267.



15 T. Zhu, Y. Song, H. Ji, Y. Xu, Y. Song, J. Xia, S. Yin, Y. Li, H. Xu, Q. Zhang and H. Li, *Chem. Eng. J.*, 2015, **271**, 96–105.

16 D. Liu, J. Wang, X. Bai, R. Zong and Y. Zhu, *Adv. Mater.*, 2016, **28**, 7284–7290.

17 J. Maruthai, A. Muthukumarasamy and B. Baskaran, *IET Nanobiotechnol.*, 2019, **13**(2), 134–143.

18 H. A. Abubshait, M. Saad, S. Iqbal, S. A. Abubshait, A. Bahadur, M. Raheel, F. H. Alshammari, N. Alwadai, H. Alrbyawi, M. A. S. Abourehab, E. B. Elkaeed, M. A. Qayyum and H. H. Somaily, *J. Mol. Struct.*, 2023, **1271**, 134100.

19 T. M. Bawazeer, *Catalyst*, 2022, **12**, 1093.

20 S. A. Ahmed and Z. S. Seddigi, *US Pat.*, US9700882B2, 2017.

21 Z. S. Seddigi, S. A. Ahmed, A. M. Nassif and M. M. Al-Thbaiti, *US Pat.*, US9944540B2, 2018.

22 M. Arellano-Cortaza, E. Ramírez-Morales, U. Pal, G. Pérez-Hernández and L. Rojas-Blanco, *Ceram. Int.*, 2021, **47**, 27469–27478.

23 Z. Wei, F. Liang, Y. Liu, W. Luo, J. Wang, W. Yao and Y. Zhu, *Appl. Catal., B*, 2017, **201**, 600–606.

24 J. Zhou, M. Zhang and Y. Zhu, *Phys. Chem. Chem. Phys.*, 2014, **16**, 17627–17633.

25 N. Huang, J. Shu, Z. Wang, M. Chen, C. Ren and W. Zhang, *J. Alloys Compd.*, 2015, **648**, 919–929.

26 S. G. Kumar and K. S. R. K. Rao, *RSC Adv.*, 2015, **5**, 3306–3351.

27 V. Vaiano, O. Sacco, D. Sannino and P. Ciambelli, *Chem. Eng. J.*, 2015, **261**, 3–8.

28 A. A. Ibrahim, R. S. Salama, S. A. El-Hakam, A. S. Khder and A. I. Ahmed, *Colloids Surf., A*, 2021, **631**, 127753.

29 M. Morad, M. A. Karim, H. M. Altass and A. S. Khder, *Environ. Technol.*, 2021, **42**, 2680–2689.

30 E. U. Mughal, A. Javaid, M. Imran, M. A. S. Abourehab, E. B. Elkaeed, N. Naeem, A. Y. A. Alzahrani, A. Sadiq and S. F. Kainat, *Inorganica Chim. Acta*, 2023, **546**, 121329.

31 Y. Wang, Q. Wang, X. Zhan, F. Wang, M. Safdar and J. He, *Nanoscale*, 2013, **5**, 8326–8339.

32 H. Liu, H. Hou, F. Gao, X. Yao and W. Yang, *ACS Appl. Mater. Interfaces*, 2016, **8**(3), 1929–1936.

33 Y. Chen, W. Huang, D. He, Y. Situ and H. Huang, *ACS Appl. Mater. Interfaces*, 2014, **6**(16), 14405–14414.

34 L. Yang, Z. Si, D. Weng and Y. Yao, *Appl. Surf. Sci.*, 2014, **313**, 470–478.

35 D. Chen, K. Wang, T. Ren, H. Ding and Y. Zhu, *Dalton Trans.*, 2014, **43**, 13105–13114.

36 Z. Liu, X. Liu, D. Lu, P. Fang and S. Wang, *Mater. Lett.*, 2014, **130**, 143–145.

37 W. Gao, M. Wang, C. Ran and L. Li, *Chem. Commun.*, 2015, **51**, 1709–1712.

38 Y. Li, B. Wang, S. Liu, X. Duan and Z. Hu, *Appl. Surf. Sci.*, 2015, **324**, 736–744.

39 K. Kalpana and V. Selvaraj, *Ceram. Int.*, 2015, **41**, 9671–9679.

40 S. Pal, S. Maiti, U. N. Maiti and K. K. Chattopadhyay, *CrystEngComm*, 2015, **17**, 1464–1476.

41 Y. Xie, H. Zhang, J. Lv, J. Zhao, D. Jiang and Q. Zhan, *Appl. Surf. Sci.*, 2022, **578**, 152074.

42 Y. Peng, H. Zhou, Y. Wu, Z. Ma, R. Zhang, H. Tu and L. Jiang, *J. Colloid Interface Sci.*, 2022, **609**, 188–199.

43 C. An, W. Jiang, J. Wang, S. Wang, Z. Ma and Y. Li, *Dalton Trans.*, 2013, **42**, 8796–8801.

44 J. Wang, P. Wang, Y. Cao, J. Chen, W. Li, Y. Shao, Y. Zheng and D. Li, *Appl. Catal., B*, 2013, **136–137**, 94–102.

45 C. Wu, *Mater. Lett.*, 2014, **136**, 262–264.

46 S. Khanchandani, P. K. Srivastava, S. Kumar, S. Ghosh and A. K. Ganguli, *Inorg. Chem.*, 2014, **53**(17), 8902–8912.

47 C. Dong, K.-L. Wu, M.-R. Li, L. Liu and X.-W. Wei, *Catal. Commun.*, 2014, **46**, 32–35.

48 M. Pirhashemi and A. Habibi-Yangjeh, *J. Mater. Sci.: Mater. Electron.*, 2016, **27**, 4098–4108.

49 H. Huang, N. Huang, Z. Wang, G. Xia, M. Chen, L. He, Z. Tong and C. Ren, *J. Colloid Interface Sci.*, 2017, **502**, 77–88.

50 M. H. T. Tung, N. T. D. Cam, D. V. Thuan, P. V. Quan, C. V. Hoang, T. T. T. Phuong, N. T. Lam, T. T. Tam, N. T. P. L. Chi, N. T. Lan, D. N. Thoại and T.-D. Pham, *Ceram. Int.*, 2020, **46**, 6012–6021.

51 Y. Cheng, L. He, G. Xia, C. Ren and Z. Wang, *New J. Chem.*, 2019, **43**, 14841–14852.

52 Y. Pan, X. Yuan, L. Jiang, H. Wang, H. Yu and J. Zhang, *Chem. Eng. J.*, 2020, **384**, 123310.

53 M. Tang, Y. Ao, C. Wang and P. Wang, *Appl. Catal., B*, 2020, **268**, 118395.

54 D. A. Reddy, J. Choi, S. Lee, R. Ma and T. K. Kim, *RSC Adv.*, 2015, **5**, 67394–67404.

55 S. K. Lakhera, R. Venkataramana, G. Mathew, H. Y. Hafeez and B. Neppolian, *Mater. Sci. Semicond. Process.*, 2020, **106**, 104756.

56 N. Güy and M. Özcar, *J. Photochem. Photobiol. A: Chem.*, 2019, **370**, 1–11.

57 J. Choi, D. A. Reddy and T. K. Kim, *Ceram. Int.*, 2015, **41**, 13793–13803.

58 S. K. Lakhera, H. Y. Hafeez, R. Venkataramana, P. Veluswamy, H. Choi and B. Neppolian, *Appl. Surf. Sci.*, 2019, **487**, 1289–1300.

59 X.-G. Zhang, D.-L. Guan, C.-G. Niu, Z. Cao, C. Liang, N. Tang, L. Zhang, X.-J. Wen and G.-M. Zeng, *Sci. Total Environ.*, 2019, **668**, 730–742.

60 J. Yi, L. Huang, H. Wang, H. Yu and F. Peng, *J. Hazard. Mater.*, 2015, **284**, 207–214.

61 J. Chen, W. Mei, Q. Huang, N. Chen, C. Lu, H. Zhu, J. Chen and W. Hou, *J. Alloys Compd.*, 2016, **688**, 225–234.

62 X. Zhang, P. Yang, Y. Bai, B. Yang and W. Liu, *Adv. Powder Technol.*, 2020, **31**, 973–985.

63 L. Wang, H. Hong, C. Zhang, L. Sun, S. Liu and S. Wang, *J. Environ. Sci.*, 2016, **41**, 112–120.

64 C. M. Magdalane, K. Kaviyarasu, J. J. Vijaya, B. Siddhardha and B. Jeyaraj, *J. Photochem. Photobiol., B*, 2016, **163**, 77–86.

65 R. Yang, G. Song, L. Wang, Z. Yang, J. Zhang, X. Zhang, S. Wang, L. Ding, N. Ren, A. Wang and X. Yu, *Small*, 2021, **17**, 2102744.

66 L. Wang, X. Tang, Z. Yang, J. Guo, Z. You, Y. Cai, X. Niu, X. Zhang, L. Zhang, J. Zhang, A. Wang, J. Liu, H. Liu and X. Yu, *Chem. Eng. J.*, 2023, **451**, 139007.



67 L. Wang, X. Zhang, X. Yu, F. Gao, Z. Shen, X. Zhang, S. Ge, J. Liu, Z. Gu and C. Chen, *Adv. Mater.*, 2019, **31**, 1901965.

68 J. Liu, J. Chen, Z. Wu, K. Zhu, J. Wang, Z. Li, G. Tai, X. Liu and S. Lu, *J. Alloys Compd.*, 2021, **852**, 156848.

69 S. Rajaboopathi and S. Thambidurai, *Curr. Appl. Phys.*, 2017, **17**, 1622–1638.

70 K. Kaviyarasu, E. Manikandan, P. Paulraj, S. B. Mohamed and J. Kennedy, *J. Alloys Compd.*, 2014, **593**, 67–70.

71 J. Ahmad and K. Majid, *New J. Chem.*, 2018, **42**, 3246–3259.

72 I. Ahemen and F. B. Dejene, *J. Mater. Sci.: Mater. Electron.*, 2018, **29**, 2140–2150.

73 P. P. Pal and J. Manam, *Radiat. Phys. Chem.*, 2013, **88**, 7–13.

74 V. Koutu, P. Ojhab, L. Shastri and M. M. Malik, *AIP Conf. Proc.*, 2018, **1953**, 030278.

75 J. H. Zheng, J. L. Song, Q. Jiang and J. S. Lian, *Appl. Surf. Sci.*, 2012, **258**, 6735–6738.

76 V. Manthina and A. G. Agrios, *Nano-Struct. Nano-Objects*, 2016, **7**, 1–11.

77 A. L. Al-Otaibi, E. Howsawi and T. Ghrib, *Nano-Struct. Nano-Objects*, 2020, **24**, 100551.

78 S. Shaker-Agjekandy and A. Habibi-Yangjeh, *Mater. Sci. Semicond. Process.*, 2015, **34**, 74–81.

79 M. Z. A. Warshagha and M. Muneer, *ACS Omega*, 2022, **7**(34), 30171–30183.

80 K. Sirohi, S. Kumar, V. Singh and A. Vohra, *Acta Metall. Sin. (Engl. Lett.)*, 2018, **31**, 254–262.

81 N. Pourshirband, A. Nezamzadeh-Ejhieh and S. N. Mirsattari, *Chem. Phys. Lett.*, 2020, **761**, 138090.

82 M. Z. A. Warshagha and M. Muneer, *Langmuir*, 2020, **36**(33), 9719–9727.

83 M. Z. A. Warshagha and M. Muneer, *Surf. Interfaces*, 2021, **26**, 101394.

84 M. Z. A. Warshagha and M. Muneer, *Int. J. Environ. Anal. Chem.*, 2020, **102**, 6339–6358.

85 X. Yuan, L. Jiang, X. Chen, L. Leng, H. Wang, Z. Wu, T. Xiong, J. Liang and G. Zeng, *Environ. Sci. Nano*, 2017, **4**, 2175–2185.

86 F. Chen, Q. Yang, J. Sun, F. Yao, S. Wang, Y. Wang, X. Wang, X. Li, C. Niu, D. Wang and G. Zeng, *ACS Appl. Mater. Interfaces*, 2016, **8**(48), 32887–32900.

87 H. I. Elsaeedy, *Mater. Sci. Semicond. Process.*, 2019, **93**, 360–365.

88 S. R. Sri Ramkumar, N. Sivakumar, G. Selvakumar, T. Selvankumar, C. Sudhakar, B. Ashokkumar and S. Karthi, *RSC Adv.*, 2017, **7**, 34548–34555.

89 M. Poloju, N. Jayababu, E. V. Rao, R. G. Rao and M. V. R. Reddy, *Surf. Interfaces*, 2020, **20**, 100586.

90 P. S. Kumar, M. Selvakumar, P. Bhagabati, B. Bharathi, S. Karuthapandian and S. Balakumar, *RSC Adv.*, 2014, **4**, 32977–32986.

91 M. Z. A. Warshagha and M. Muneer, *Environ. Nanotechnol. Monit. Manag.*, 2022, **18**, 100728.

